Anatomy of a Flash Flood in a Hyperarid Environment: From Atmospheric Masses to Sediment Dispersal in the Sea

Akos **Kalman**[a,b,c], Timor **Katz**[b], Miklos **Vincze**[e], Jake **Longenecker**[c], Alysse **Mathalon**[d], Paul **Hill**[d], Beverly **Goodman-Tchernov**[a]

[a] *University of Haifa, Department of Marine Geosciences, Leon Charney School of Marine Sciences, Mt. Carmel, Haifa 31905, Israel*

[b] *Israel Oceanographic and Limnological Research, P.O.B 8030, Haifa 31080, Israel*

[c] *University of Miami, Rosenstiel School of Marine, Atmospheric, and Earth Science, 4600, Rickenbacker Causeway, Key Biscayne, 33149, FL, USA*

[d] *Dalhousie University, Oceanography Department, 1355 Oxford Street, P.O.B 15000, Halifax, Nova Scotia B3H4R2, Canada*

[e] *HUN-REN Institute of Earth Physics and Space Science, Sopron, H-9400, Hungary*

Correspondence to: A. Kalman (akoss.kalman@gmail.com)

Highlights

1. A hyperarid desert flash flood is described and documented *in situ* from its meteorological development to arriving into the offshore

2. Flood triggered by weak polar vortex, amplified Rossby wave, causing intense rainfall in Eilat

3. Flood discharged 25,000 tons of sediment within freshwater outflow, altering salinity and sediment concentrations in the sea

4. Sediment dispersal outflow alternated between hypopycnal and hyperpycnal flows due to shifting flood dynamics and related sediment concentrations

Keywords

flood dynamics, hyperpycnal flow, amplified Rossby wave, sedimentary record, Red Sea

Abstract

Flash floods in rivers near hyper-arid coastlines impact both land and marine environments, from recharging groundwater and supporting desert ecosystems to affecting marine water quality, organisms, and substrates. Few studies, however, have followed these events from atmospheric origins to marine effects. This study tracked a desert flash flood in October 2016 in Eilat, capturing stages from atmospheric conditions to sediment distribution at sea. Observations included satellite data, meteorological reports, floodwater discharge, and sediment levels from the Kinnet Canal outlet, alongside offshore turbidity and salinity data. Our findings indicate that a weakened polar vortex amplified a Rossby wave, triggering convective instability over the Eastern Mediterranean and northern Red Sea. In Eilat (mean annual rainfall = 27 mm, SD = 21 mm), 128% of the average fell within hours, with the flood reaching the sea approximately 50 hours later and lasting 27 hours. Around 25,000 tons of sediment were discharged, causing offshore salinity drops (up to 1.75‰ below the seawater background) and fluctuations of suspended sediment concentrations due to varying flow rates. In turn, particle dispersal in the sea switched several times between hypopycnal (surface) and hyperpycnal (bottom) flows. These findings link the different stages of the flood and their cascading effects from air masses to sedimentary processes in the sea.

1   Introduction

1.1   Background

A large portion of continental shelf sediments in the shallow offshore originate from terrestrial sources delivered through rivers (Syvitski et al., 2005). In higher precipitation regions it arrives primarily through large perennial rivers, while in drier climates, such as deserts, fluvial sediments are often delivered via ephemeral rivers during sporadic precipitation events that may produce flash floods (Cohen and Laronne, 2005).

Flash flood events are crucial for both sustaining desert terrestrial ecosystems (Gee and Hillel, 1988; Hereford et al., 2006) and enriching marine systems with essential nutrients and sediments, thereby altering the physical, chemical, and biological dynamics of coastal shelf ecosystems (Hickey et al., 2010). Rainfall in desert regions is typically short-lived, sometimes robust, spatiotemporally sporadic, and capable of evolving into flashfloods (Sharon, 1972). From a human perspective, these floods may cause property damage, loss of life, and disruptions to transportation and other infrastructure (Haggag and El-Badry, 2013). For instance, between 1900 and 2016, 39 severe floods in the Middle East – spanning Egypt, Israel, Jordan and Saudi Arabia – caused over 1500 fatalities and directly impacted around 300,000 people (de Vries et al., 2018).

Historically, cities along hyperarid coastlines were rare, but this has changed dramatically in recent decades (Neumann et al., 2015). Technological advancements, including desalination plants, air-conditioned buildings, and refrigerated freight containers, have facilitated the growth of cities worldwide in these less habitable locations (Barragán and de Andrés, 2015; Holdren and Ehrlich, 1974; Small and Nicholls, 2003). However, despite these advances, flood risk due to their relative rarity and unpredictability, remains an issue.

Flood forecasts generally rely on predictions of heavy precipitation, yet in hyperarid areas, rainfall is highly variable. This variability complicates the ability to predict whether the accumulation of runoff from different adjacent catchments will lead to coastal flashfloods, thereby posing challenges for early warnings and preparations in low-lying coastal cities (Cools et al., 2012). Understanding the specific processes and conditions that lead to, or do not lead to, flashflood and related fluvial sediment discharge is essential for improving forecast accuracy and flood preparedness.

90   Principally, in arid coastlines, the deposition of fluvial sediment into the sea represents

91   the culmination of a series of interconnected events. These stages can be summarized as

92   follows: 1) atmospheric conditions leading to precipitation, 2) the occurrence of precipitation,

93   3) the drainage of water through the watershed, 4) the formation of flash floods, 5) the

94   transportation of water and sediments to the coastline, 6) the discharge of these elements from

95   the coastal outlet into the sea, and 7) the subsequent dispersal and deposition within the

96   marine environment (Cohen and Laronne, 2005; Kalman et al., 2020, 2022; Katz et al., 2015;

97   Mathalon et al., 2019; Mulder et al., 2003; Reid and Frostick, 1987). While aspects of these

98   stages have been the subject of research (Allison et al., 2012; Blum and Törnqvist, 2000;

99   Merz et al., 2021; Mullenbach and Nittrouer, 2000), comprehensive studies tracing the entire

100   sequence for a specific event are lacking. Developing a framework that traces the entire

101   sequence of events during a single flood can serve as a model for understanding similar

102   processes in other arid coastal systems, even when only partial or less detailed data are

103   available. Such a methodology could enhance our broader understanding of sediment

104   dynamics and support environmental management, ecological conservation, urban planning in

105   coastal deserts, and natural hazard assessment.

106   The aims of this study were 1) to capture the full sequence of a desert flood from

107   meteorological precursors to eventual sediment discharge from an ephemeral coastal river and

108   its dispersal in the sea; 2) to assess the dependence or relationship between parts of the

109   sequence and their outcomes, and 3) to track and identify specific atmospheric antecedent

110   conditions that contributed to the triggering mechanism of the flash flood.

111   To achieve these aims, we integrated records from regional meteorological data with

112   in-situ environmental measurements of salinity, turbidity, temperature, and surficial water

113   velocity preceding and during a flash flood event that discharged into the northern Red Sea /

114   southern Negev Desert of Israel.

115

116

117

 1.2   Previous Atmospheric and Precipitation studies

119   For decades, there has long been an interest in the linkages between meteorological

120   conditions and resulting floods (El-Fandy, 1948). One of the earliest studies on

121   meteorological trends and flooding was conducted by Ashbel (1938), who described several

122   extreme precipitation and flooding events in Rutbah, Damascus, the Dead Sea and the Sinai

123   Peninsula. The events occurred with the northward propagation of the Red Sea Trough, and

124   descending cold air from the north.

125   At present, based on nearly 70 years of data reanalysis, the RST is 96% originated

126   from Sudan (Almazroui et al., 2016), and is known to be the most active during the autumn

127   and winter (Alpert et al., 2004a; Saaroni et al., 2020). Also, it is usually accompanied by

128   upper-level westerlies or by an anticyclonic flow (Tsvieli and Zangvil, 2005); but under these

129   conditions the RST is a dry system with no rain. Southeasterly winds blow the air over the

130   sandy basins of Saudi Arabia, Iraq, and Syria, a process that often triggers aeolian transport of

131   sediment towards the Eastern Mediterranean (Dayan et al., 2008). However, no single

132   synoptic feature is solely responsible for the development of heavy rainfall over the Levant.

133

134   Kahana et al. (2002) labeled a thunderstorm producing RST as an 'Active RST'

135   (ARST). Krichak and Alpert (1998) outlined a sequence that leads to the formation of these

136   storms: moisture transport from equatorial Africa (1), followed by convection (2), and

137   intensification of The Subtropical Jet Stream (3) thus enhancing RST expansion (4) and

138   related moisture (5) towards the Levant. A detailed analysis of a severe October 1997 ARST

139   event by Dayan et al., (2001) confirmed stages (2), (3) and (5). Other studies (Dayan et al.,

140   2001, 2021; Kahana et al., 2002; De Vries et al., 2013; Ziv et al., 2005) emphasize the

141   significant role of mid-latitude upper-level troughs in amplifying instability and driving

142   rainfall.

143   Ziv et al. (2022) identified climatological precursors for cyclogenesis associated with

144   the RST extending toward the Levant. Using automated cyclone tracking (Hochman et al.,

145   2020; Ziv et al., 2015) from 1979 to 2017, they identified four patterns of upper-level trough

146   approaching the Eastern Mediterranean: 1) a cyclone crossing the Levant from the southwest,

147   2) a trough from the northeast, 3) a trough from the west, and 4) scenarios without upper-level

148   support. Notably, in the second category, intense rainfalls occured, driven by cold advection

149   resembling a polar intrusion, which greatly increases static instability over the Levant.

150

1.3   Runoff and flood development in the hyperarid GAE

151

152   Short-lived, but intense rainfall sometimes occurs over the terrestrial drainage in the
153   hyperarid landscape surrounding the Gulf of Aqaba-Eilat (GAE). Within hours, this water
154   runoff may accumulate in the otherwise dry riverbeds (wadis), and if the water volume that
155   accumulates is large enough, it can produce a flashflood. Lack of vegetation and poor soil
156   development with low permeability (Cohen & Laronne, 2005 and references therein) also
157   contributes to the prompt development of floods. The time between rainfall and initiation of
158   the flooding depends on storm intensity, duration, catchment size and which part of the
159   catchment receives the rain. Because of the temporally sporadic nature of the rain events,
160   sometimes years can pass between consecutive events in the same drainage system. These
161   extended non-flood periods allow for surface weathering processes to dominate (and dust to
162   settle), leaving ample sediment available when rains do arrive (Cohen and Laronne, 2005a).
163   Therefore, the emerging floods have high concentrations of suspended sediment that may
164   even increase towards the terminal basins owing to transmission loss (Shentsis et al., 2001).

165   A sequence of instrument gauge stations was first installed in the southern Arava
166   desert in 1966, set along ephemeral streams such as Nahal Yael (2 km long, 0.6 km^2
167   catchment area) that lead into larger tributaries (Schick and Lekach, 1993). These gauges have
168   provided information regarding flow and sediment loads, demonstrating that sediment
169   discharge is inconsistent. For example, during 33 years of monitoring, 14 years lacked any
170   flow, and 8 years had flood events during which the flow terminated prior to the gauge at the
171   lowest elevation (Clapp et al., 2000). The measured floods that terminated before reaching the
172   sea delivered large amounts of sediment to the wadi system (100 tons of eroded sediment per
173   km^2 per year (Schick and Lekach, 1993), 460 tons of sediment in a single event (Clapp et al.,
174   2000)). In this local hyperarid wadi, total suspended solids (TSS) during flooding were
175   measured at 44 grams per liter, based on an average from three flash floods (Lekach and
176   Schick, 1982). This concentration is very high relative to averages recorded in large perennial
177   rivers such as the tropical Amazon (0.19 grams per liter), Mississippi (0.82 grams per liter)
178   (Milliman and Farnsworth, 2013), or pre-Aswan Nile River (3.43 grams per liter) (Shalash,
179   1982).

180

1.4   Recent GAE Flood Research

182   Eilat, a coastal city established in 1951 with an increasing population of greater than

183   55,000 people (population 50,000 reported in by Azaryahu, 2005; and 55,000 reported in

184   www.worldpopulationreview.com, accessed in 2025) is located in the northernmost part of

185   the GAE immediately west of the neighboring city of Aqaba, Jordan which is home to over

186   150,000 residents (Arieli, 2021). Both Eilat and Aqaba expand significantly (> one million

187   visitors) during holiday seasons with tourists arriving to enjoy attractions like the world's

188   northernmost tropical coral reefs (Loya, 2004; Xilotl Soberon And Rofe 2017).

189   Floods in the GAE can form within hours after rainfall affects the Kinnet watershed in

190   the northern GAE (**Fig. 1**). The Kinnet Canal (**Fig. 2**) serves as a conduit for the Kinnet

191   watershed, channeling both water and sediment loads (predominantly in suspension) toward

192   the lowest elevation point. When the arriving water volume from the catchment area is

193   substantial enough, floods can make their way into the sea (Katz et al., 2015b).

194
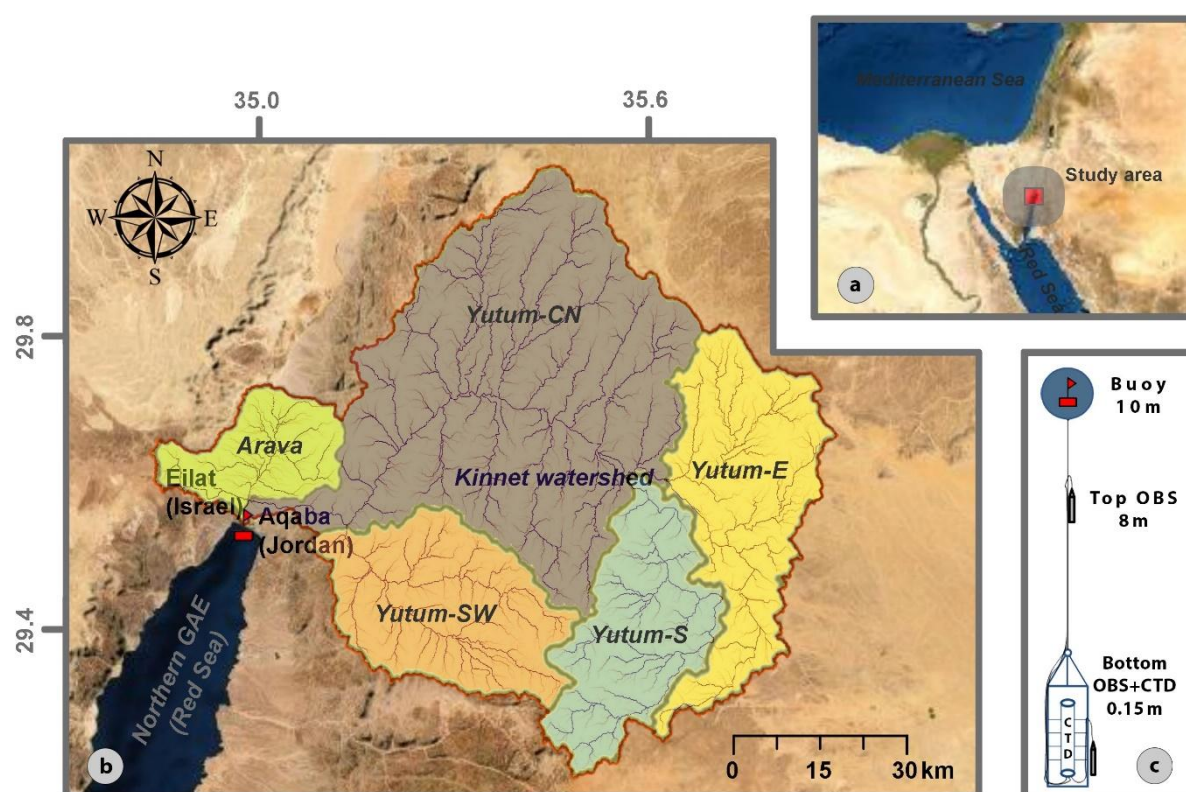
195
196   **Fig. 1.** a) Regional map showing the location of the head of the GAE. (b) Local map illustrates the mooring's
197   position along with ephemeral river systems. The delineation of streams transporting water and sediment to the
198   northern shelf of the GAE is represented by the brown lines. Although all runoff ultimately converges at a single
199   outlet, the Kinnet Canal, dividing the watershed into subbasins helps to identify distinct source areas and
200   improves the estimation of flood arrival at the river mouth (Eilat city center). Maps adapted from Kalman et al.,
201   2020 (c) Schematic drawing of the mooring station setup (Sea Bird Electric CTD and Campbell Electric 3+ OBS
202   sensors), positioned 250 m offshore the Kinnet outlet at 13 m water depth.
203

204 Flash floods reaching the sea through the Kinnet Canal (discharge located on Eilat shoreline)

205 have been documented since 1994 (Kalman et al., 2020b). Between 1994 and 2012, events

206 were dominated by small to mid-scale floods, intermixed with extended dry periods (Kalman

207 et al., 2020b; Katz et al., 2015b). In 2006, Aqaba was struck by an exceptionally large flood,

208 causing extensive damage (Farhan and Anbar 2014). Historical records also describe

209 significant weather events, including a "terrific rain and hail storm that literally washed away

210 half of modern Aqaba in 1940", and a storm on 11 March 1966, classified as a 50-year return

211 period event (Farhan and Anbar, 2014).

212   The west (Eilat) and the east (Aqaba) sides of the head of the Gulf have different flood

213 potentials. The Wadi Yutum catchment on the east is 4867 km^2, nine times larger than the

214 Arava catchment on the west, and its higher elevation (~1600 m) increases water flow speed

215 and sediment transport. The northern part of Wadi Yutum catchment possesses several sinks

216 and sabkhas in the north, but rainstorms in the rocky southern slopes send water towards

217 Aqaba and the GAE (Farhan and Anaba, 2016). The smaller Arava catchment (458 km^2 and

218 lower elevation (~500 m) still generate floods during rainstorms in the nearby Eilat

219 Mountains.

220   In the northern GAE, Katz et al. (2015) documented a hyperpycnal plume created by a

221 flashflood's high-density sediment load discharging into the sea. Their study characterized the

222 floodwaters (temperature, salinity, sediment concentration) along the coastline and within the

223 plume as well as the sediments deposited on the seafloor. They identified the distribution and

224 thickness of the flood sediments and estimate the volume discharged (approximately 20,000

225 tons), concluding that floods are the most dominant source of GAE seafloor sedimentation.

226 Subsequent investigations explored bioturbation (Mathalon et al., 2019), Late-Holocene

227 climate reconstructions (Kalman et al., 2020b), and anthropogenically-driven changes in

228 sediment dynamics (Kalman et al., 2022).

229

230

2   Data and Methodology

Throughout the study, meteorological data and weather reports surrounding the GAE were closely monitored in order to be 'at ready' in the case of an opportunity to analyze an arriving flash flood. Given that the likelihood of floods occurring in a given day in the year is less than 0.5% (Kalman et al., 2020b), it was unknown whether any floods would actually occur during the designated observational period. Moreover, because of this low likelihood, it was understood that there was a high likelihood that the study could entirely miss an opportunity to make direct measurements, observations, and collections. To counter this issue, the study combined the use of a mooring station that collected regular interval measurements *in situ,* and a multi-person field team, equipped at all times with a field sampling set ready for arriving for taking field measurements if a flash flood occurred (**Fig. 2**). After (if) a flood occurred, the meteorological conditions preceding the production of the flash flood were analyzed in higher resolution. The following describes the methodological sequence performed from the identification of a potential flood event to field measurements, offshore deeper measurement casts, retrieval of mooring array data, and higher resolution meteorological analysis.

248

249 **Fig. 2.** Flash flood entering the northern Red Sea following a heavy precipitation event on 28 October, 2016.

250 Photo by Gal Eyal.

251

2.1 Meteorological data

253 The synoptic analysis in this study, used to track precipitation centers, was based on two data

254 sources. One of these on a regional scale was the Precipitation Estimation from Remotely

255 Sensed Information using Artificial Neural Networks (PERSIANN) dataset (Nguyen et al.,

256 2019), obtained via CHRS Data portal, with a 0.5° x 0.5° resolution. Additionally, in a local

257 scale, NASA's Global Precipitation Measurement (GPM) Integrated Multi Satellite Retrievals

258 (IMERG) with a 0.1° x 0.1° resolution, were utilized to compensate for the lack of dense

259 meteorological network in the trans-national Kinnet watershed, located at the northernmost tip

260 of the Gulf of Eilat-Aqaba. Given the region's hyperarid conditions and limited gauging

261 systems, satellite-derived precipitation data were essential for accurately estimating

262 precipitated water.

263 The GPM's IMERG data is pivotal in this research due to its advanced capabilities in

264 providing high-resolution precipitation estimates, which are particularly crucial in regions

where conventional meteorological infrastructure is sparse or non-existent. The GPM constellation and ground validation suite employ a host of sensors including the active Dual-frequency Precipitation Radar enabling precise measurements of rain rates (Masaki et al., 2014) and the passive GPM Microwave Imager essential for measuring precipitation intensity and distribution (Draper et al., 2015). Following data collection, a series of steps, including ground validation (Tapiador et al., 2020), are undertaken to ensure the accuracy and reliability of the precipitation estimates (Huffman et al., 2020). The subsequent merging of data from various sources, complemented by rigorous quality control and validation procedures culminates in the final IMERG datasets (Huffman et al., 2020).

In the specific case of the Kinnet watershed, the utilization of IMERG datasets are necessary, and used alone, because physical meteorological stations are sparce. The two stations (Eilat, Israel and Aqaba, Jordan) present in the watershed are only 10 kilometers from one another, and show nearly identical annual average precipitation values (*Jordan Meteorological Department, Israel Meteorological Service*, Katz et al., 2015). Therefore, they are not useful for measuring the overall contribution of rainfall for the entire watershed. This absence of adequate ground-based meteorological stations and gauging systems in this hyperarid region makes satellite-derived data the most reliable source for the accurate assessment of precipitation patterns. The integration of this high-resolution, satellite-based data with the NCEP/NCAR reanalysis imagery offers a comprehensive understanding of the hydrological dynamics within this trans-national watershed.

2.2   Time series mooring station

An instrumented mooring station was anchored ~250 m offshore in front of the Kinnet Canal at a depth of 13 m. The instruments on the mooring array included a Sea Bird Electronics SBE 19plus v2 CTD (temperature, salinity, depth) positioned 0.15 m above the seafloor, and three Campbell Electric OBS 3+ optical backscatter sensors calibrated with pure, local flood sediments collected from slackwater deposit near the outlet, and attached to the instrument line at three different depths (0.15m, 2m, 8m) above the seafloor 250 m offshore. Calculations for sediment concentration based on turbidity values from the OBS 3+ sensors was calculated using values derived from direct calibration of sediments from this site (see Mathalon et al. 2019 methods and description). The mooring station instruments collected the properties of the water column for a period of 9 months between April, 2016 and January, 2017. In moored mode, data was collected with a temporal frequency of 300 seconds with 4 measurements per

sample. During the mooring period, instruments were cleaned and examined roughly every 10 days by scuba divers, data was retrieved, and the batteries were recharged.

2.3   Canal measurements

The research team collected a series of measurements and samples from the Kinnet Canal outlet during active flooding (e.g. October 28, 2016 event). Flow speed (m s^{-1}) was calculated based on the surface speed obtained from time a drifting object traveled a predetermined distance (30 meter), corrected (multiplied) by 0.6 to account for riverbed friction due to roughness and riverbed geometry at the measured sequence of the flood (Chie, 1992). Water samples were collected every ~ three hours from the centerline of the waterflow to calculate sediment concentration (g l^{-1}). Similarly, at regular intervals the flood level at the banks was recorded and after the flood had finished, the cross-section areas of the Canal (m^2) for each 3-hour interval were calculated (**Supplementary fig. 1**).

2.4   Suspended alluvium major element analysis

Major elements (Fe, Al, Mn) were measured from the canal flood water collections. To do this, approximately two grams of dried (60 °C) sediment per sample was ground and homogenized with a mortar and pestle to a powder and analyzed in a vacuum chamber using an ED-XRF (Spectro Scout). The measurements were calibrated with 3-8 certified sediment standards as described in Zirks et al., (2021).

2.5   Stream order and watershed delineation

Hydrological modeling of the Kinnet watershed was performed 1) to understand the time lag between the cessation of rain and initiation of flooding at the river outlet; and 2) to describe hydrological behavior and structure of river system in case of flood events. Digital elevation models (DEMs) from the Shuttle Radar Topography Mission (SRTM) were downloaded (https://earthexplorer.usgs.gov/) and processed in a series of steps (fill, flow direction, flow accumulation, basin, stream order) using the Hydrology tool (Bajjali, 2017) in ArcGIS Pro (v3.1). This step delineates streams that possess significantly higher potential for flood related hazards.

3   Results

During the study period, a major flash flood event that reached the sea was observed in the last week of October 2016. The results below are presented as a sequence of the event that includes 1) the analysis of mesoscale convective systems during this period, leading to 2) a heavy rainfall and 3) flash flood development with 4) high quantities of transported material in the southern Negev Desert that eventually 5) discharged from the Kinnet Canal to the tip of the northern Gulf of Aqaba-Eilat, Red Sea. The meteorological antecedent conditions leading up to the event were then assessed to consider possible unique features associated with flood production on a regional scale.

3.1   Kinnet Catchments

The hydrological analysis of the landscape shows that the Kinnet watershed is the largest among sub-catchments that direct water and sediment into the head of the northern GAE. Modeling performed by incorporating DEM data from satellite imagery delineated two major watershed basins; west (Arava catchment) and east (Yutum catchment) from the pull-apart basin (Wadi Arava) in between. The Yutum catchment is larger in size and, based on topography, can be further subdivided into four sub-basins, contributing uniquely to the overall hydrological dynamics of the hyperarid watershed (Fig 1).

3.2   Meteorological Antecedent conditions (Sept 20 – Oct 27)

The initial northward propagation of the Sudan Monsoon Low over the Red Sea (also known as the 'Red Sea Trough', RST) towards the Eastern Mediterranean was first detected 37 days before heavy precipitation event that ultimately led to a relatively large flash flood in Eilat. Rather than representing a continuous synoptic feature, this period comprised a series of RST-related disturbances with a trough axis retaining in the region and intermittently re-intensifying. Particularly, the RST strengthened on the 24th (3 mb over 9 mb), 3 days prior to the massive rainfall (**Supplementary fig. 2**). Congested clouds developed above Ethiopia beginning on Oct 5, but there was no significant formation of clouds until Oct 24th above and in the vicinity of the Red Sea.

On the 24th, various atmospheric conditions prevailed in the Middle East. At first, velocities of the Polar Front decreased significantly. Based on 200 hPa vector wind map of the day, no sign of a continuous Polar Jet in the region prevailed whatsoever. Satellite

imagery shows however a narrow, but long – stretching cloud formation around 22-23°N across the Red Sea and the Arabian Peninsula, in addition to scattered congested clouds above the Southern Red Sea. The 200 hPa vector wind composite confirms that the clouds were formed as a result of enhanced velocities of the STJ (**Supplementary fig. 3**). On Oct 18th, STJ velocities varied between 25-30 ms^{-1}, located at the border of Chad-Lybia-Egypt-Sudan through the Red Sea towards the Middle East. Its shape elongated in east-west direction and its velocity intensified up to 43 ms^{-1} by the 22nd, became the strongest at the difluence over the northern tip of the Persian Gulf. Later, the position of the STJ gradually moved southward and reached its southernmost position on Oct. 27 above the Red Sea at 15-16°N, before moving back northward after the storm.

At low atmospheric levels, warm advection that had been formed previously above Sudan and Ethiopia prevailed, resulting in a six-degree temperature rise to 33°C in the center of the Red Sea Trough. Simultaneously, a -9°C and 35% relative humidity (5°C less and 20 % more humid than ambient) upper-level trough reached the Middle East from northwestern direction.

These differential warming and cooling effects enhanced static instability with respect to normal conditions. The majority of the moisture (RH=80-90%) to the EM was transported at 700 hPa from tropical Sudan and Ethiopia. During the transport, relative humidity continuously increased in the Levant with no significant change of the temperature profile, which resulted in lowering of the lifting condensation level, embedding to a deep convection above the entire region. Clouds were forming along the fringing mountains at the southern part of the Red Sea on the 25th, but no precipitation occurred.

3.3 *Mesoscale convection*

While the RST was approaching the Middle East from the south at low (near sea) atmospheric levels, the well-developed upper-level trough (atmospheric Rossby wave), pointing southwest, formed over the Eastern Mediterranean. As a result, a cold convection took place on the 25th that turned to advection leading to a formation of a cold front over the EM. The combination of lower-level convergence and upper-level divergence are fundamentally linked to enhanced potential for the initiation of intense, but spatially spotty rainstorms due to the topographic heterogeneity of its mountainous local desert environment (El-Fandy, 1950). At the tip of the cold front, advection lifted the airmass above the border of Libya and Egypt and increased the relative humidity from 30% to 65% at 850 hPa geopotential height (gph). The

394   wind vectors at 700 hPa gph showed that in addition to this humid air was transported towards

395   the Red Sea, the intensified STJ prevailed and effected NE movement of airmasses located in

396   lower atmospheric levels (**Supplementary fig. 4**). On the 26th,12.00 pm, congested clouds

397   were formed above the mid-Red Sea and heavy rainfall began ~1000 km south from Eilat

398   (**Supplementary fig. 5)**.

399   During the morning of Oct 26, a cloud system of approximately 480 km in diameter

400   was formed above Sinai-southeast Jordan and northwest Saudi Arabia axis. The cloud system

401   developed at the contact zone of the west side of the east pointing RST and the east side of the

402   upper-level trough that occupied the EM at higher atmospheric levels. The rain cells were

403   formed over the ridges along the leeside of the Red Sea mountains, moved further to the

404   middle of the sea, then drifted northward by the RST. Within 18 hours at 0600 UTC 27

405   October 2016, showers and rainstorms were registered from the entire Negev desert (*Israel*

406   *Meteorological Service*).

407   The tip of the RST on the 27th of October reached Cyprus and Syria, its deepest

408   penetration into the Eastern Mediterranean portion of the Middle East. Polar Jet velocities at

409   ~31N latitudes gradually increased, and on this day showed its strongest phase (45 m s^{-1} in the

410   center) and turned 45 degrees, already pointing northeast, reconnecting the opened high-

411   altitude wind system.

412   The center of the upper-level trough moved from the Nile delta to mid-Egypt within

413   two days (27 Oct), narrowing the contact zone of four (upper-level trough, Red Sea Trough,

414   Polar Jet, and Subtropical Jet) mesoscale systems to approximately 200 km wide channel in

415   the Eastern Mediterranean (**Fig. 3**). As a result, precipitation centers reached the north of the

416   Eastern Mediterranean, but also penetrated further into continental Syria and Iraq. A section

417   of the cold upper-level trough disconnected from the main body of the trough on the 27th,

418   creating a giant 'cold ball' like feature above Eilat, which accelerated its mixing with the near

419   sea level spreaded and warm RST. The northeast-pointing Polar Jet carried and dissipated the

420   trough away and by the end of the day on 28 October, the pressure differences between the

421   atmospheric layers equalized, resulting in the end of the storm.

422

423
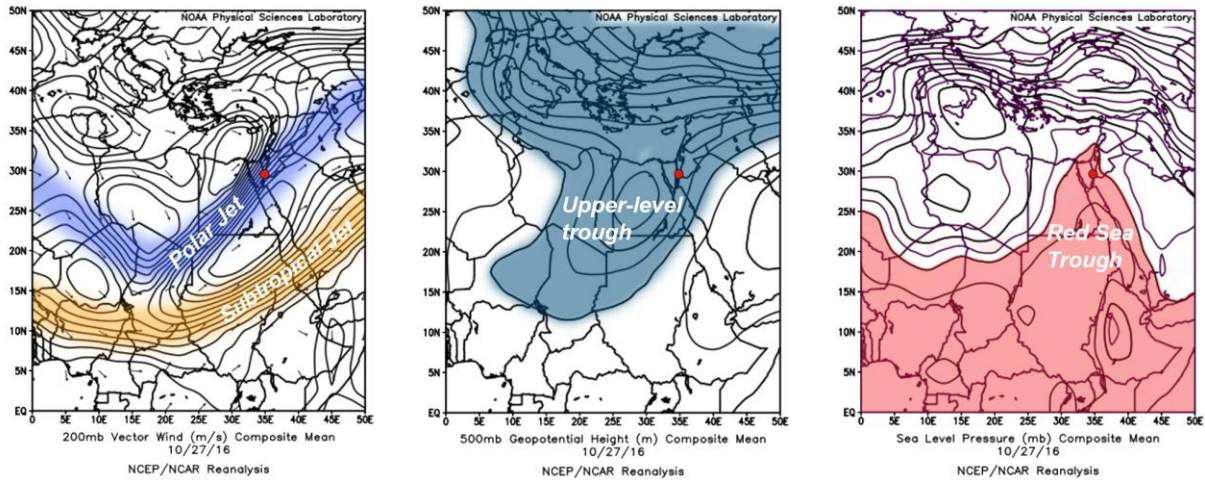
Fig. 3: Composites on the heavy rainfall in Eilat (red dot) showing three mesoscale systems (Polar Jet, Subtropical Jet, upper-level trough) and a synoptic scale system (Red Sea Trough) in which their fourfold contact zone narrowed down to ~200 km wide gap over the Eastern Mediterranean contributing to the formation of the historical flashflood.

3.4   Precipitation and Flashflood entering the sea

A flash flood reached the head of the GAE at ~3:00 am October 28th, 2016; after an Active RST accompanied by scattered showers and thunderstorms made contact with a high-pressure belt over the mid-latitudes and inundated the Middle East region from Egypt, through Israel, Jordan, as well as Lebanon and Syria. The RST moved from the mid to the northern Red Sea within 18 hours. During this time, nearly every segment of the 4867 km^2 Kinnet watershed received some amount of precipitation (**Fig. 4**), which eventually contributed to the formation of a flash flood. The total precipitated rain during this time was calculated at 133 million m^3 in the Kinnet catchment, accumulating for ~51 hours prior to the flashflood's arrival into the GAE.

439

440
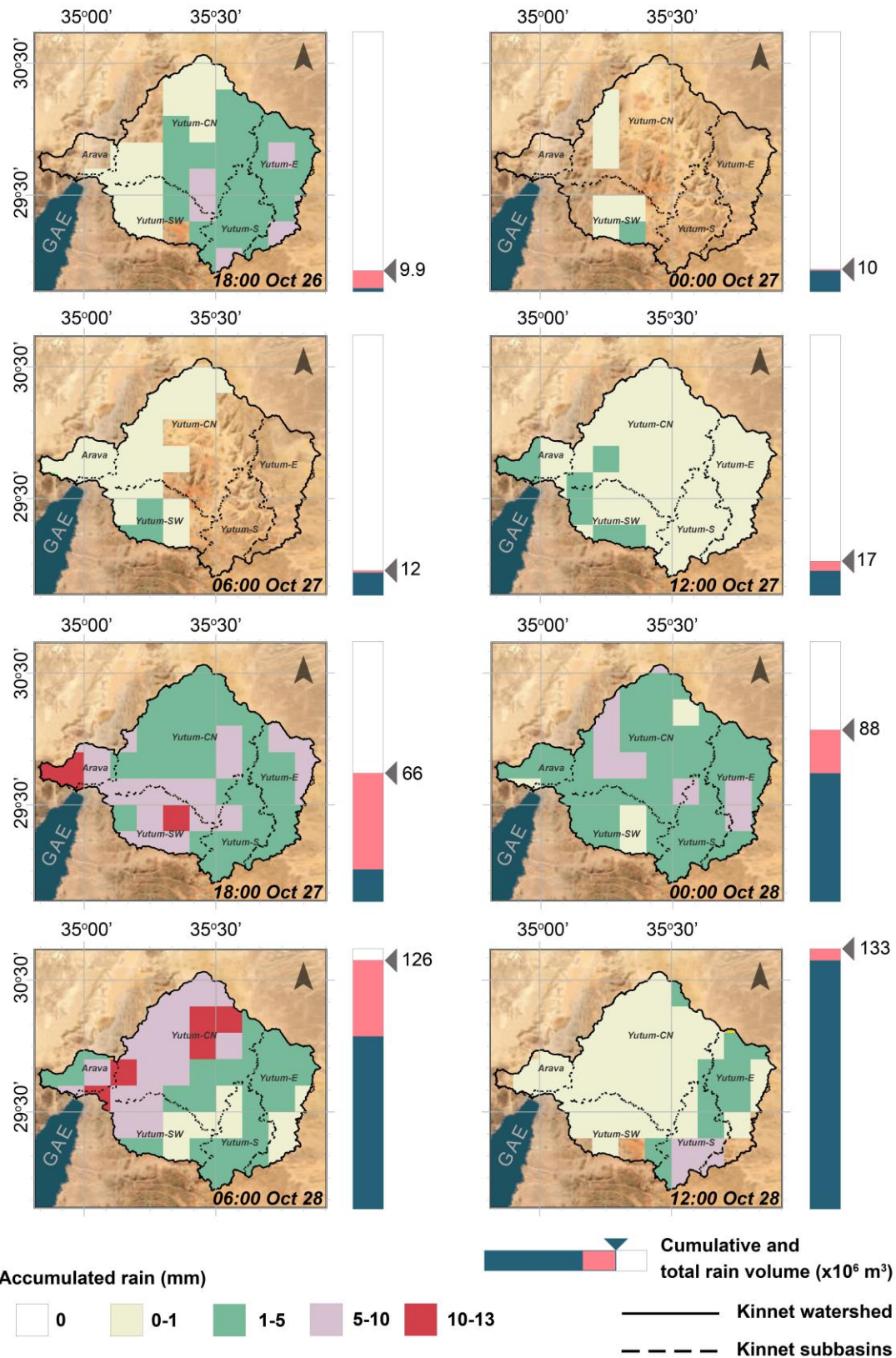
Fig. 4: GPM-IMERG satellite precipitation showing 6h rain development in the Kinnet watershed in 0.1°
x0.1°resolution. Accumulated rain during hours between measurements (red bar) and total accumulated rain
volume (blue +red bars) indicate that the majority of the water precipitated within only 18 hours.

444

445 During the precipitation period, rain was temporally and spatially unevenly distributed. For

446 the first 24 hours, scattered and localized rain events in the catchment area resulted in the

447 arrival of a total of 17 million m^3 water (~13 % of the total). In the following 18 hours

448 however, both sides of the Arava Valley (Eilat and Wadi Yutum catchments) experienced

449 intense storms, adding 109 million m^3 water (~82% of the total). The last 6 hours resulted in

450 an accumulation of an additional 7 million m^3 rain water (~5% of the total), but similarly to

451 the initial phase of the event, it was spatially spotty and mostly precipitated in the eastern side

452 (Yutum-S, Yutum-SE) of the watershed. It was followed by a 6-hour no precipitation period,

453 before precipitating only ~52.000 m^3 rain (0.04%) at both spatially and temporally highly

454 varied stages.

455 According to conversations with witnesses, some flood waters arrived at the head of

456 the GAE after the middle of the night, around 3 AM on the 28th of October (see **Fig. 5**), but no

457 turbid water, only elevated discharge was described. The research team performed the first

458 recording and sampling at 9AM and continued to take 8 measurements for 30 hours.

459

460

461
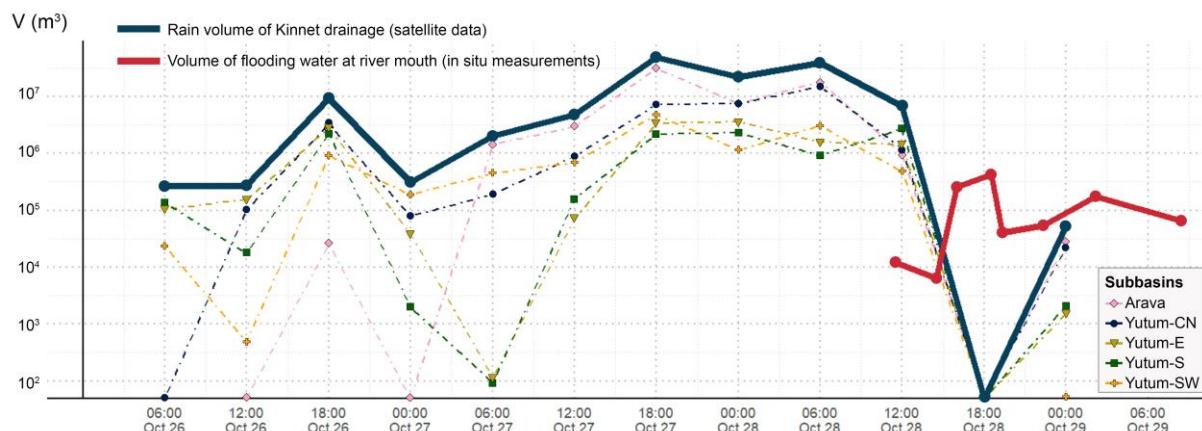
462 **Fig. 5.** Summary of quantitative analysis of the water before and during flooding on the 28th of October, 2016 in

463 Eilat based on satellite data and in-situ measurements. The distribution of the rain amongst the subbasins (dashed

464 lines) indicate the patchy nature (unevenly distributed) of rain events in this hyperarid environment at the first 36

465 hours of the storm, which was followed by concentrated and elevated quantities of rainfall in all subbasins.

466 According to witnesses, the flash flood arrived at the sea at 9 o'clock in the morning and transported large

467   quantities of suspended sediment over a period of 30 hours.

468

469

470

471

472 The water flow and the sediment concentrations of the flood increased from 1.33 m^3 s^{-1} and

473 20.73 g l^{-1} at 9 AM to 47.42 m^3 s^{-1} and 20.91 g l^{-1} at 2:30 PM, respectively. By 6:30 PM the

474 flow decreased to 13.53 m^3 s^{-1} and the sediment concentration increased to 27.55 g l^{-1} and by

475 2:30 AM in the next day the flow was further reduced to 2.87 m^3 s^{-1} and the sediment

476 concentrations rose to a 33.5 g l^{-1}. In total, 1.04 * 10^6 m^3 water flowed into the sea through the

477 Kinnet Canal and transported 2.44 *10^4 tons of sediment over approximately 30 hours, which

478 the majority of this quantity was then deposited on the shallow marine shelf. The sea surface

479 discoloration from transported sediments was visible for as long as 7 days. Estimations

480 extrapolated from the elemental analysis of the samples taken during the event suggest that

481 1014 tons of Fe, 1413 tons of Al, and 20 tons of Mn entered the sea.

482 Indications of the arriving flood waters were also recorded by the offshore mooring

483 station instruments (**Fig. 6**). According to the sensors, water temperature did not change, but

484 water salinity and turbidity started to fluctuate at 9:50 AM on the 28th of October, 2016, 250

485 m offshore the canal outlet. These two parameters mirrored one another, as salinity dropped

486 turbidity rose and vice versa. Ten minutes after midnight, turbidity increased to as high as

487 2.18 g l^{-1} sediment concentration, and salinity near the seafloor dropped to 38.73 PSU, a value

488 that is 1.80 PSU less than the mean salinity (40.53 PSU) recorded over the 9 months of

489 observations from this site. During the last stage of the flood, salinity returned to just below-

490 background values 6 hours after its lowest measured value (~40.4 PSU), while turbidity was

491 still highly variable. Later, this variance with minimal amplitudes was limited only to the

492 bottommost conditions and remained diversified hours after the cessation of the flood.

493
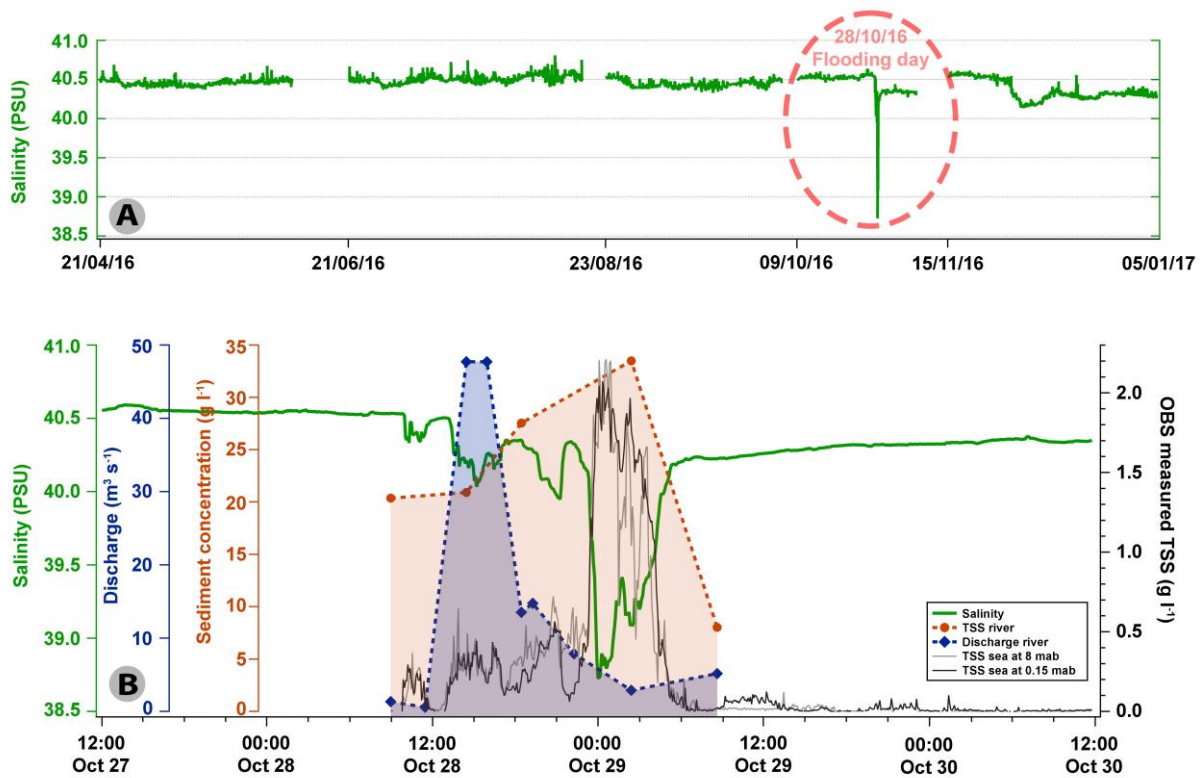
Fig. 6. Offshore mooring array measurements (A and B) and Kinnet water and sediment discharge collection and recording results including the flood event of October 28, 2016. A) Nine months of salinity measurements from the mooring station. The flooding event is clearly visible as a sudden decrease in salinity. No significant temperature change was registered during the event. Gaps in the data indicate the periods during which the instruments were removed for downloading data and maintenance. B) On-land measurements of changing of the flood discharge and sediment concentration over time, and expanded view of three days of mooring station measurements (TSS and salinity) including immediately before and after the flooding event. The OBS turbidity sensors from the 3 m depth (top) and 0.15 m depth ('bottom') both show fluctuations and increases coinciding with the arrival of flood water.

4   Discussion

This study followed the sequence of a storm that occurred on 28 October, 2016 in Eilat from its initial phase to and through a flash flood that started deposited alluvium in the northern Red Sea a day later. The flood was the 13th flood recorded since records began in 1994 (Katz et al., 2015; Kalman et al., 2020). From 1994 to 2012, there was a drought period wherein flood occurrence was below one per year (0.17), followed by increased occurrence of 1.7 floods per year (2012-2020). With regard to the hazard level of the 28 October 2016 flood event, no death occurred, nor was property damage reported; and transportation and infrastructure (roads and airport) were not affected. The interpretation of reanalysis data revealed that multiple unstable atmospheric conditions led to the formation of the storm that within a day exceeded the annual average precipitation in Eilat. It began with the northern propagation of the RST three days prior to actual flash floods forming in the southern Negev. Tropical moisture was transported towards the Red Sea and enhanced velocities of the Polar Jet and intensified RST expansion towards the Eastern Mediterranean. At the same time, a well-developed upper-level cold front approached the Eastern Mediterranean and the combination of lower-level convergence and upper-level divergence initiated an intense rain event associated with thunderstorms.

4.1   *Storm analysis and implications*

At sea level, the RST as one of the key elements in the formation of the storms is one of the main synoptic patterns that influence weather in the Levant region (Alpert et al., 2004b). The northward propagation of this low-pressure system is not a rare case; RST is formed 43.7% of the days between October and November during the rainy season (Saaroni et al., 2020). This means that RST is present roughly every second day during these months, providing the potential for heavy precipitation to form. Saaroni et al. (2020) developed an algorithm that identifies the northern part of the RST and classifies it according to the location of the trough axis with respect to longitude 35°E. This classification is important because RST expansion and orientation influences the distribution of a possible storm over the Levant in its "active" (ARST) phase (Kahana et al., 2002).

Hochman et al, (2021) used CMIP5 climate projections to categorize winter RSTs and analyzed their characteristics and impacts on the region. They found that rainfall associated with wet RST (WRST) is projected to decline by 37% by the end of the 21st century due to shifts in atmospheric circulation patterns, increased temperatures, and a reduction in the

frequency and intensity of WRST events. Additionally, they found that extreme precipitation events related to the WRST show distinct atmospheric pattern differences when compared to lighter precipitation events within the same system (Hochman et al., 2023).

Ziv et al., (2005) showed a December 1993 ARST example with flooding wherein a persistent southerly flow from over the Red Sea prior to the event (in addition to tropical moisture transport) induced air ascendance along the Red Sea, and carried it to the surrounding regions. During the October 2016 case, however, two days prior to the flood, at the tip of the upper-level trough, advection lifted the airmasses above the border of Libya and Egypt (westward of the study area) and increased the relative humidity by 35%, which was then transported towards the Red Sea. Such elevated air moisture values fit those used in Krichak et al., (2012)'s algorithm for identifying ARST events. They concluded that high moisture content in the air influences the intensity of the developing storm in the Eastern Mediterranean; and conversely, drier air masses along the Eastern Mediterranean coasts reduces the possibility (and intensity) for an ARST event. The conditions observed during this 2016 event support the presence of an ARST event. In some rare cases, the lowest flank of the upper-level trough can disconnect from the meandering mid-latitude upper-level low system; and can form into an individual cut-off low resulting in a negative upper-level temperature anomaly. This is extremely favorable for thunderstorms in the atmosphere and can lead to and induce fatal flashfloods on land (Dayan et al., 2021).

At upper atmospheric levels, major mid - and high latitude cyclonic and anti-cyclonic systems affect the atmospheric Rossby waves (e.g. extension, direction and persistent time of upper-level troughs and ridges), and it is the cold upper-level trough introduced from northern regions that enhanced convective instability during the October event. A negative phase of the North Atlantic Oscillation created an amplified Rossby wave three days prior to the flood, resulting in two upper-level troughs extending southward: one in the Western Mediterranean up to latitude 17 degrees and one in the Eastern Mediterranean up to latitude 15 degrees. Because of a weak polar vortex, the cold air from the arctic region (from Scandinavia in the case of the eastern type) could escape, creating a hole in the Ferrel cell that cut through the Polar Front, and triggered the ARST event (**Video-1**). Since the polar vortex began to strengthen again on the 25th, enhanced velocities of the Polar Front "arrived" to the EM, and in the absence of the Polar Front, ran into the Subtropical Jet stream. By the following day, the enhanced high altitude wind pushed STJ at least 2 degrees further south, meanwhile Polar Jet winds bounced back from this mid-latitude waveguide (Branstator, 2002) and further enhanced its velocities in the following days. Similar conditions were described in southwest

573 Asia by Saligheh, (2021); and concluded that pulling the Polar Jet southward that merges into
574 the Subtropical Jet stream can enhance cyclogenesis and lead to hydrodynamic instability.
575 Asiri et al., (2020); studied specifically the STJ over Africa and the Middle East and found
576 based on nearly 60 years of reanalysis data that its north-south shifting is controlled by the
577 temporal extension of the Azores High and the Siberian High. When the Azores High is
578 weakened or shrank westward, the STJ shifts southward; and when the Siberian High is
579 weakened or shrank eastward, the STJ shifts northward. This is in agreement with the October
580 2016 event. Prior to the Eilat flooding, the Azores High weakened and the STJ track gradually
581 shifted southward and its position only changed direction when the Azores High was
582 beginning to increase.
583

4.2 From precipitation to flow into the sea

585 During the October 2016 flooding event, the Kinnet watershed received 133 million m^3 rain
586 although most of the rain precipitated on the Jordanian mountains in the Wadi Yutum
587 catchment (**Fig. 4**). Rainfalls in the desert are typically described as short lived and intense
588 (Sharon, 1972); under extreme conditions they have been recorded as delivering ~110 mm
589 within 3 hours (Youssef et al., 2016). This is certainly true for observations made in singular
590 locations; whereas the satellite measurements show the overall lingering presence of the
591 event.
592   The timing from the onset to final cessation of rainfall (including initial 12 hour
593 minimal precipitation period and a 6-hour gap) was 66 hours. During that time, floods were
594 produced within the wadis in the watershed. Rain cells above the Kinnet watershed initially
595 developed only in its eastern side, then later on in the entire watershed, and in some cases
596 significantly larger amounts precipitated in the vicinity of Wadi Arava and Yutum-CN
597 subbasin (**Fig. 1b**). This flood was most likely facilitated by the first rain period that pre-
598 soaked the ground (13% of the total precipitation), but it is likely the second rainy spell that
599 provided the runoff that ultimately ended in the discharged flood water as the majority of the
600 rain precipitated within the following 18 hours (82% of the total precipitation).
601
602 After the cessation of the rain, wadis continued to receive runoff which flowed downslope
603 towards the outlet of the Kinnet Canal and the sea. This flow reached the sea approximately
604 50 hours after the rain started, and roughly 3 hours after most of the rainfall ended.
605

606   Unfortunately, in the poorly monitored (very low spatial dispersion of gages and
607   weather stations) catchment area of the October 2016 event it was not possible to assess the
608   transmission losses of the precipitated water. To overcome this issue and give an estimation of
609   water loss from the formation of the rain until water discharge at the river mouth, we used
610   GPM-IMERG precipitation data that has been shown to correlate well with precipitation
611   gauge data both in humid (Pradhan et al., 2022; Yang et al., 2018) and arid regions (Chen et
612   al., 2020; Mohammed et al., 2020). It is important to note that its 0.1° x 0.1 ° spatial
613   resolution (10x10 km grid) does not allow to analyze precipitation accumulated in wadis and
614   lower ranked streams specifically (which is important because same rain event can cause
615   flooding in a particular wadi, while the neighboring wadi remains dry), making the
616   quantification of the patchy nature of a hyperarid rain event impossible; its 30 minute
617   temporal resolution however enables to capture the sum of the precipitated water and give us
618   the confidence to apply its dataset on the nearly 5000 km^2 Kinnet watershed. We calculate
619   that approximately 133 million m^3 precipitated in the entire watershed of the Kinnet Canal
620   during this event and that ~1 million m^3 (0.75 %) of it ultimately reached the GAE through
621   the Kinnet Canal. This limited yield reflects the fact that runoff from more distant parts of the
622   watershed (particularly from the eastern sub-basins) faces greater losses due to longer travel
623   distances, allowing for increased infiltration and evaporation. The ~99% difference reflects
624   infiltration relating to a complex matrix of soil properties and variations in rain intensity,
625   duration, location and evaporation. In arid regions where sequential gage measurements were
626   conducted, transmission loss rates showed considerable variations. For example, 13.2 % in an
627   Australian desert stream (Dunkerley and Brown, 1999) up to 98% in parts of Saudi Arabia
628   (Walters, 1990); and in between 20% and 85%, located in Nahal Zin, Israel's Negev Desert
629   (Greenbaum et al., 2001).

630   GPM data stretches back 21 years and gives us the opportunity to investigate which areas in
631   the watershed have high(er) probabilities for the water to accumulate (**Fig. 7**). The 2000-2021
632   window in Eilat covers 12 years from a prolonged drought period (1994-2012) characterized
633   by three flashfloods only, and a more humid 8-year period (2012-2020) with the occurrence of
634   12 flashfloods in total (Kalman et al., 2020).

635
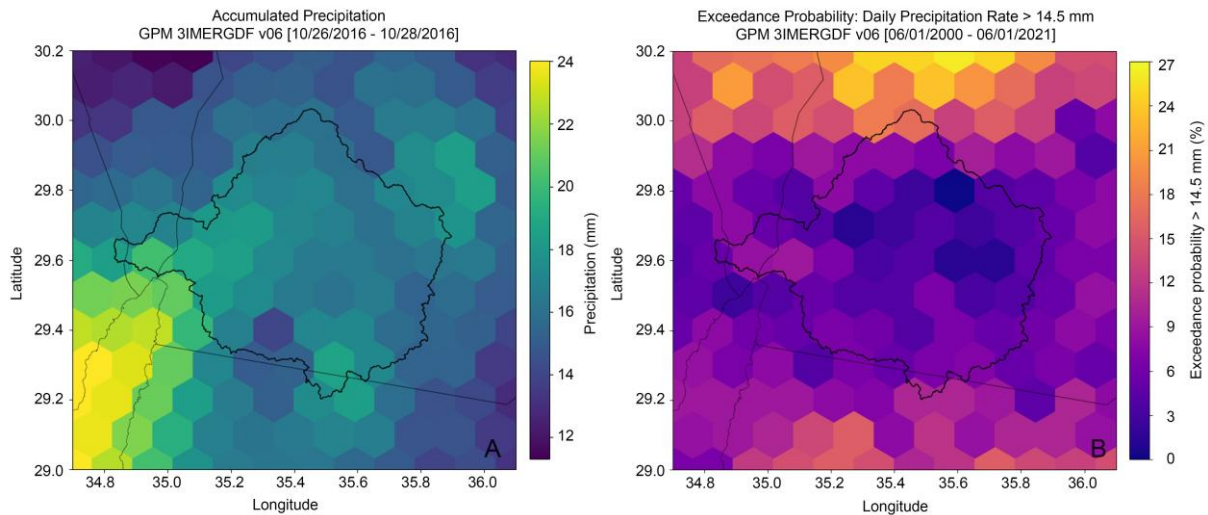
Fig. 7. GPM-IMERG data visualized in the Kinnet watershed at the head of the Gulf of Aqaba-Eilat, Red Sea. A) Sum of accumulated rain preceding a flashflood on 27 October, 2016. B) Sum of accumulated rain preceding a flashflood on 27 October 2016. (B) Likelihood of precipitation exceeding 14.5 mm. This threshold corresponds to a local flashflood event recorded on 1 March 2017, when 14.5 mm of rain fell in under 3 hours and temporarily flooded the streets of Eilat. This threshold was used to assess flashflood potential across the basin. Likelihood values represent the proportion of days with precipitation exceeding 14.5 mm relative to the total number of days during the analyzed period (2000–2021).

Fig.7A shows the sum of precipitated water within the Kinnet watershed that preceded the formation of the Oct 27, 2016 flooding event in Eilat. The main accumulation centers during the event were around the surroundings of Wadi Arava and within the Yutum-center sub-basin. Because of the hypersensitivity for extreme weather events of the region, there is a great variety in the distribution of the rainwater that describe each precipitation event. Therefore, the accumulated precipitation case is rather a description of this particular event than an analog to generalize the distribution of the precipitation during any flashflood events.

On March 1, 2017, a small flashflood was generated after a hailstorm directly affected the Eilat mountains. The accumulated water in Eilat gauge station was 14.5 mm (54% of the yearly total) that precipitated within 3 hours. Streets were flooded and closed quickly, but also were reopened within an hour, because rain water was not sufficient enough to induce waterflow in Yutum ephemeral riverbeds that, if it had occurred, would arrive with a lag to the Kinnet outlet and to its surroundings. Because the rain event was local and could trigger a flashflood, its precipitation (14.5 mm) was used as a threshold value to calculate exceedance probabilities for the Kinnet watershed (**Fig.7B**). The highest probabilities for exceeding the threshold value can be found around the Wadi Arava, the southern Jordanian mountains and the northern part of the Yutum-center subbasin. On the other hand, in the center of the

662 Yutum-center subbasin, the likelihood of exceeding the threshold value is near zero. The

663 southern probabilities may be explained by the orographic effect, which forces the RST to

664 flow over high topography as well as the northern probabilities may be explained by the

665 interannual position of the diffluence of the upper-level trough interacting with the RST, and

666 resulting in explosive cyclogenesis (Kouroutzoglou et al., 2015; Ziv et al., 2022).

667

4.3   Sediment dispersal at sea

669 Based on the flow and sediment concentrations in the Kinnet canal we calculated that during

670 the October 2016 flashflood, approximately 24,000 tons of suspended sediment entered the

671 sea. This value likely and slightly underestimates the true total, as measurements were not

672 available during the initial onset and possibly the waning stage of the flood. Nevertheless, the

673 estimate captures the main body of the event and is representative of the overall magnitude.

674 The amount is similar to the reported 21,000 tons of suspended sediment transported to the

675 GEA from the Kinnet Canal during the Feb 2013 flash flood event (Katz et al., 2015). In both

676 cases the amount far exceeded the annual airborne dust introduced into the northern Gulf of

677 Aqaba-Eilat (Chen et al., 2008). From shallow water sediment cores Katz et al. (2015)

678 roughly estimated average of circa 10 kg sediment per meter square coverage of the alluvium

679 on the seafloor primary deposition zone after a historical flooding in February 2006, which

680 magnitude corresponds with 6 kg sediment on average per meter square coverage produced by

681 the October 2016 event.

682   When desert floods arrive into the sea, if their sediment concentrations are high

683 enough, their bulk density becomes higher than that of the seawater and they are expected to

684 produce hyperpycnal flows that plunge and progress along the seafloor as turbidity currents

685 (Katz et al., 2015). This high sediment load drags fresher water beneath saltier water layers

686 that would otherwise float above the saltier, denser seawater. If however, sediment

687 concentrations are not high enough and the bulk density of the discharged floodwater is lower

688 than that of the seawater, they form hypopycnal plumes that disperse at and near the sea

689 surface. Notably, in some cases hypopycnal flows can generate turbidity currents due to

690 trickling down (fingering) and amassing of suspended sediments near the seafloor (Parsons et

691 al., 2001).

692   According to witnesses, the Eilat flood arrived to the sea at 3 AM on the 28th of

693 October, however the mooring data registered the initiation of salinity decrease and turbidity

694 increase only at 9.50 AM in the morning, ~ 7 hours later. If these reports are correct, then this

695   time lag between visual notice and instrumental registration suggests either low sediment

696   concentrations in the discharged water at this initial stage that caused only a hypopycnal

697   plume or a very slow ($\sim$1 cm s^{-1}), offshore progression of the mixed flood water. It was also

698   possible that the witnesses in the darkness observed higher discharge without significantly

699   elevated sediment concentration, which water might have originated from a nearby

700   desalination factory. With no measurements from the station at this time, this question

701   remains open. Flood related turbidity at the measuring station lasted from 9.50 AM Oct 28

702   until 5.15 PM Oct 29 and the increased turbidity was registered at approximately the same

703   time in the 0.15 and 8 mab sensors (**Fig. 6**). This would suggest that by the time floodwater

704   reached the station they were already mixed (though not homogeneously) in the water

705   column. During the $\sim$31 hours of the registered event, salinity and sediment concentrations at

706   the measuring station mirror-imaging one another demonstrating considerable fluctuations

707   near the seafloor (**Fig. 6**). Taking into consideration that there is some lag between the outlet

708   and the measuring station, these fluctuations were likely caused by changes in floodwater and

709   sediment discharge from the Kinnet canal. Such fluctuations would result from changes in the

710   intensity and geographical distribution of the rainfall at the catchment area, many hours

711   earlier. At its peak, salinity at the moored station was reduced to 38.75 ‰ which is

712   approximately 1.75 ‰ less than the measured salinity in the 7 months of measurements prior

713   to the event. This drop is 19 times greater than the standard deviation of the salinity observed

714   during that period. This drop clearly demonstrates that the freshwater arriving with the

715   flashflood was denser due to its high sediment load, and therefore was forced downward

716   rather than being distributed on the water surface. The drop coincided with the highest TSS to

717   salinity ratios suggesting a concurrent increase in sediment concentrations in the discharged

718   floodwater (**Fig.8a**).

719

720
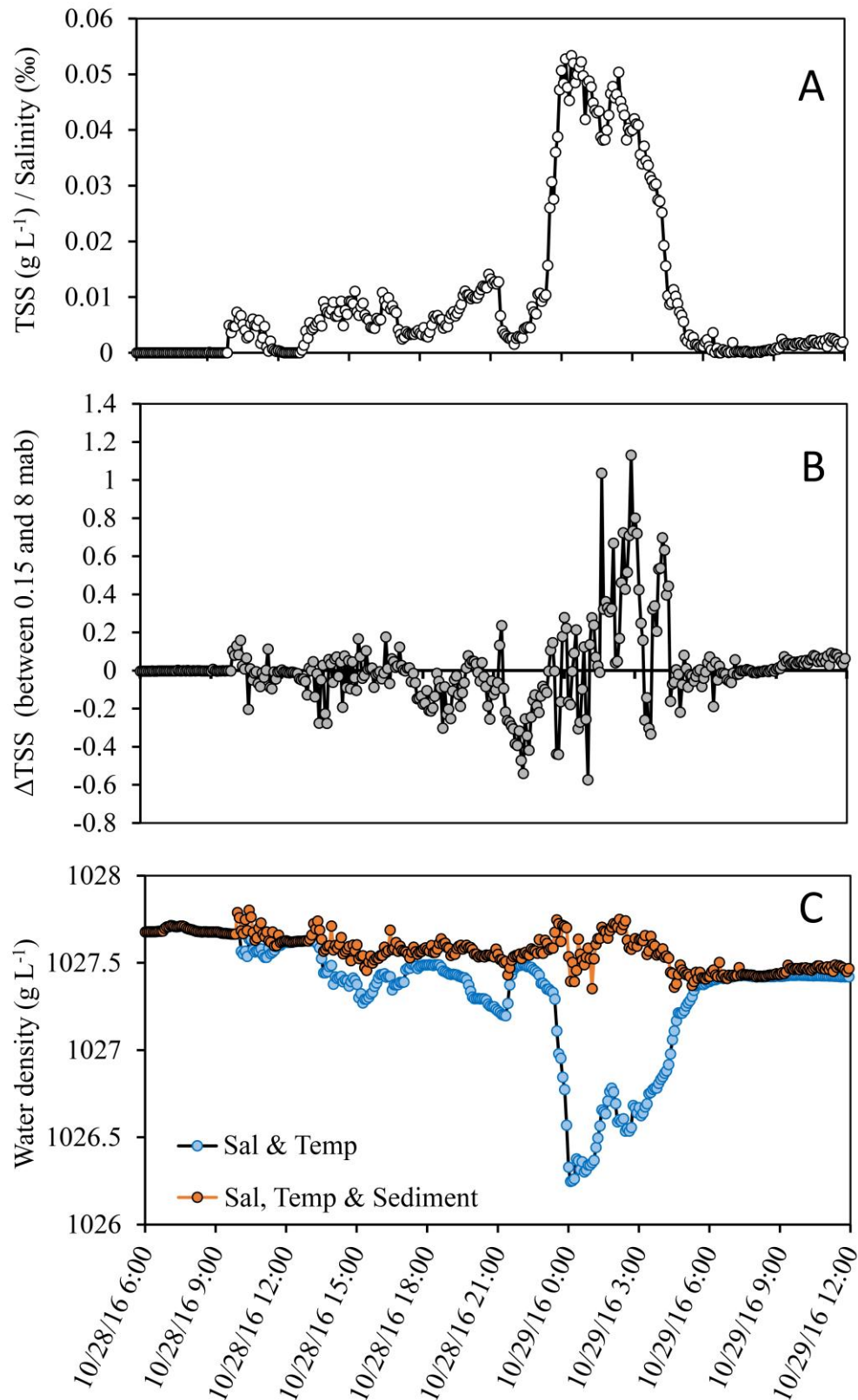
Fig. 8. Measurements of an offshore mooring station of the Oct 27, 2016 flashflood event that reached the sea in the northern Gulf of Aqaba-Eilat. The floodwater discharged with low salinities loaded with high concentrations of suspended sediments to the sea (A), resulted in both hypo- and hyperpycnal plumes (B), and elevated bottom water densities (C) during the evolution of the flood.

726 Moreover, during this and three prior, though much smaller events, sediment concentrations

727 near the seafloor (0.15 mab) were higher than those measured at 8 mab, (**Fig.8b**). Although

728 floodwater and sediments were found throughout the water column at the station area early

729 on, these measurements indicate intermittent occurrences of hyperpycnal flows during this

730 time. This assumption is supported by calculated density of the bottom water, based only on

731 the temperature and salinity and then after correcting it with the suspended sediment

732 concentrations (assuming mean sediment particles density of 2.65 g cm^{-3}). The results, shown

733 in **Fig. 8c** demonstrate that the freshening of the seawater alone would have greatly reduced

734 the bottom water density, causing it to float. However, when corrected with the suspended

735 sediment concentrations, the bulk density of the near bottom water occasionally exceeds that

736 of the undiluted seawater, enabling it to plunge and progress as a hyperpycnal flow. Even

737 more so, when considering the gradual decrease in the salinity (and hence density) of the

738 water column offshore the Kinnet outlet during the flood which further decreased the

739 incoming floodwater buoyancy. Notably, in the 5, discrete measurements of sediment

740 concentrations that were made in the Kinnet Canal during the flood, the highest value was

741 33.5 g l^{-1}. This value is considerably less than the required ~43 g l^{-1} to cause direct

742 hyperpycnal plumes in the head of the GAE (Katz et al., 2015b). We therefore expect that at

743 the beginning of the floods, convective fingering of sediment from above may have caused

744 smaller hyperpycnal events near the seafloor (Parsons et al., 2001). Conversely, the major

745 hyperpycnal flow that was registered at the marine station between 11:00 pm Oct 28th and

746 4:30 AM Oct 29th was likely caused by direct plunging of dense flood water. This would

747 suggest that sometime around 2:00 am between the 3rd and 4th TSS measurements, sediment

748 concentrations in the Kinnet may have reached the required minimum threshold (36-43 g/l) to

749 generate a hyperpycnal plume upon entering the GAE. Sediment concentration measurements

750 at the outlet during both the 3rd and 4th collections were around 15-fold higher relative to the

751 marine station 250 m offshore. These values record the process of both dilution with seawater

752 and sediment dispersal as the suspected plume traveled along the seafloor. It is therefore

753 reasonable to assume, given the relatively low sediment concentration values recorded (2.18

754 g/l) at 250 m offshore that the proposed hyperpycnal plume dissipated before reasing the

755 station's sensors. While a hyperpycnal plume may not have been present at that distance,

756 sediment dispersal continued in the form of near-bottom transport, possibly enhanced by

757 added sediment entrained in the turbulent flow. Salinity returned to near background levels by

758 5:45 AM Oct 29, and remained at ~ 40,3 PSU, ~0,2 PSU less than average until the retrieval

759 of the mooring 9 days after the flood event.

760

761 *4.4   Storms, Rain, Flashfloods, and Planning*

762   In this study, we show how climate and sediments are related. The synoptic analysis of

763 the storms illustrate what key parameters contribute to the triggering mechanism of a storm

764 and where in the particular watershed is likely to rain. Using reanalysis data, all these

765 parameters can be collected for each flood event and a database can be formed. When

766 flooding, large quantities of sediments from the catchments can be transported to the sea,

767 where they may serve as a climate archive. Although sediments upon arriving to the sea in the

768 northernmost GAE undergo different levels of post-depositional processes that alter their

769 physical-chemical properties; by recognizing changes in flood deposit signatures, it is

770 possible to reconstruct past climatic variations on the seafloor downcore (Kalman et al., 2020,

771 2022; Katz et al., 2015). Just as atmospheric parameters are catalogued in synoptic analyses,

772 the physical and chemical properties of flashflood sediments in their depositional settings can

773 be compiled into the same database, linking atmospheric triggers with sedimentary responses.

774 While the use of machine learning requires large datasets, we propose that in locations where

775 distinct flood layers are consistently preserved (potentially hundreds of well-characterized

776 sediment-climate pairs), such datasets could be developed and applied to train machine

777 learning models. It is expected that the combined analysis of climatology, hydrology and

778 sedimentology of flash flood events will help to better understand the interlinkages between

779 the otherwise separately discussed aspects of flood hazards in hyperarid regions (**Fig. 9**).

780 Furthermore, it will impose careful site selection and proper planning in the establishment of

781 new coastal cities and already existing cities planning to expand.

782

783
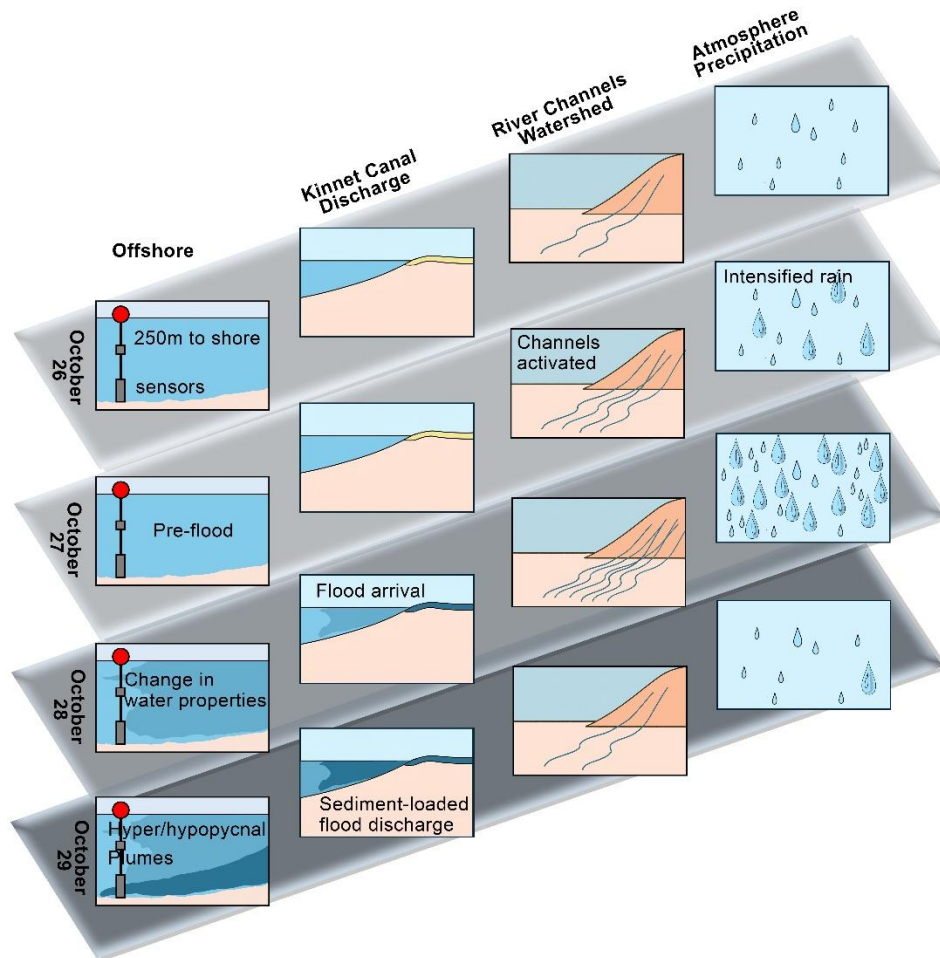
Fig. 9: Sequence of sediment transport processes during the October 2016 flash flood in Eilat.
The figure illustrates daily changes from October 26–29, 2016, showing the evolution of sediment
transport from precipitation to offshore deposition in the northern Red Sea. It details concurrent
developments in offshore waters, at the canal discharge point, within the watershed, and includes
rainfall intensity for each day. The seven key stages include: (1) atmospheric conditions conducive to
precipitation, (2) precipitation events, (3) watershed drainage, (4) flash flood formation, (5) sediment
and water transport to the coastline, (6) discharge at the coastal outlet, and (7) marine dispersal and
deposition.

792

5 Conclusions

A hyper arid region flashflood event was studied from its preceding meteorological conditions, precipitation, run-off development, and ending with its arrival into the Gulf of Eilat-Aqaba. It was observed that a negative phase of the North Atlantic Oscillation triggered an amplified Rossby wave, whereas its lower flank reached the Levant region and created thunderstorms leading to an exceptional 3-day long rain event in Eilat, Israel. The precipitation was unevenly distributed in the watershed, and needed 51 hours to reach the Kinnet canal outlet. Only 0.75 % of the precipitated water reached the sea eventually. Sediment transport into the sea during this single event far exceeded annual airborne dust precipitation. Both hypo- and hyperpycnal plumes during the flood event were instrumentally captured. It is concluded that meteorological and climate precursors are the earliest to identify actual environmental conditions, and since precipitation and sedimentation are linked, flash flood born sediment in marine deposits can provide a key to identifying paleoclimatic trends that together can serve as basic input for developing early warning systems against flash floods and related hazards.

6 Data availability

The data supporting the findings of this study is available from the corresponding author upon reasonable request.

7 Video supplement

The video supplement (Video-1) illustrating the visualization of cold air escaping from the Arctic region and triggering the ARST event is attached to this manuscript as *Video-1-Kalman-et-al.gif*."

8 Author contribution

Conceptualization: AK, TK, PH, BGT

Data curation: AK, TK, MV, JL, BGT

Formal analysis: AK, TK, MV, JL

Investigation: AK, AM

Methodology: AK, TK, AM, PH, BGT

Visualization: AK, TK, MV, JL, BGT

Writing – original draft preparation: AK

Writing – review & editing: AK, TK, MV, JL, AM, PH, BGT

Supervision: TK, BGT

Resources: TK, PH, BGT

Project administration: AK, TK, BGT

Funding acquisition: TK, PH, BGT

9 Competing interests

The authors declare that they have no conflict of interest.

10 Acknowledgement

The research was funded by the Schulich Foundation Canada-Israel Collaboration Project, the Ministry of Interior, Israel and the Yohay Ben-Nun Foundation NAF-IOLR. The authors thank the Interuniversity Institute for Marine Sciences Eilat for general support and members of the Institute who contributed during *in situ* sampling of the flash flood in harsh and sometimes dangerous conditions. We thank Professor Hadas Saaroni for her thorough and precious feedback. Special thanks to Eyal Amitai, Emanuel Sestieri, Erez Levin, Asher Meir, Ofir Hameiri, Sivan David, Gabriele Guerrini, Gal Eyal, and Guilhem Banc-Prandi.

11 References

Allison, M. A., Demas, C. R., Ebersole, B. A., Kleiss, B. A., Little, C. D., Meselhe, E. A., Powell, N. J., Pratt, T. C., and Vosburg, B. M.: A water and sediment budget for the lower Mississippi–Atchafalaya River in flood years 2008–2010: Implications for sediment discharge to the oceans and coastal restoration in Louisiana, J. Hydrol., 432–433, 84–97, https://doi.org/https://doi.org/10.1016/j.jhydrol.2012.02.020, 2012.

Alpert, P., Osetinsky, I., Ziv, B., and Shafir, H. (2004a): Semi-objective classification for daily synoptic systems: Application to the eastern Mediterranean climate change, Int. J. Climatol., 24, 1001–1011, https://doi.org/10.1002/joc.1036.

Alpert, P., Osetinsky, I., Ziv, B. and Shafir, H. (2004b), A new seasons definition based on classified daily synoptic systems: an example for the eastern Mediterranean. Int. J. Climatol., 24: 1013-1021. https://doi.org/10.1002/joc.1037

Arieli, T.: Aqaba and Eilat: Twenty-five years of 'good neighborly relations' in a post-conflict environment, in: Twin Cities across Five Continents, Routledge, 133–146, 2021.

Ashbel, D.: Great floods in Sinai Peninsula, Palestine, Syria and the Syrian Desert, and the influence of the red sea on their formation, Q. J. R. Meteorol. Soc., 64, 635–639, https://doi.org/https://doi.org/10.1002/qj.49706427716, 1938.

Asiri, M. A., Almazroui, M., and Awad, A. M.: Synoptic features associated with the winter variability of the subtropical jet stream over Africa and the Middle East, Meteorol. Atmos. Phys., 132, 819–831, 2020.

Awad, A.M. and Almazroui, M., 2016. Climatology of the winter Red Sea trough. Atmospheric Research, 182, pp.20-29, https://doi.org/10.1016/j.atmosres.2016.07.019

Azaryahu, M.: The beach at the end of the world: Eilat in Israeli popular culture, Soc. Cult. Geogr., 6, 117–133, https://doi.org/10.1080/1464936052000335008, 2005.

Bajjali, W.: ArcGIS for environmental and water issues, Springer, 2017.

879   Barragán, J. M. and de Andrés, M.: Analysis and trends of the world's coastal cities and

880   agglomerations, Ocean Coast. Manag., 114, 11–20,

881   https://doi.org/10.1016/j.ocecoaman.2015.06.004, 2015.

882

883   Blum, M. D. and Törnqvist, T. E.: Fluvial responses to climate and sea-level change: a review

884   and look forward, Sedimentology, 47, 2–48, https://doi.org/https://doi.org/10.1046/j.1365-

885   3091.2000.00008.x, 2000.

886

887   Branstator, G.: Circumglobal teleconnections, the jet stream waveguide, and the North

888   Atlantic Oscillation, J. Clim., 15, 1893–1910, 2002.

889

890   Chen, C., Chen, Q., Qin, B., Zhao, S., and Duan, Z.: Comparison of different methods for

891   spatial downscaling of GPM IMERG V06B satellite precipitation product over a typical arid

892   to semi-arid area, Front. Earth Sci., 8, 536337, 2020.

893

894   Chen, Y., Paytan, A., Chase, Z., Measures, C., Beck, A. J., Sañudo-Wilhelmy, S. A., and Post,

895   A. F.: Sources and fluxes of atmospheric trace elements to the Gulf of Aqaba, Red Sea, J.

896   Geophys. Res. Atmos., 113, 1–13, https://doi.org/10.1029/2007JD009110, 2008.

897

898   Chie, Y. Ben: Dimensionally Homogeneous Manning's Formula, J. Hydraul. Eng., 118,

899   1326–1332, https://doi.org/10.1061/(ASCE)0733-9429(1992)118:9(1326), 1992.

900

901   Clapp, E. M., Bierman, P. R., Schick, A. P., Lekach, J., Enzel, Y., and Caffee, M.: Sediment

902   yield exceeds sediment production in arid region drainage basins, Geology, 28, 995–998,

903   https://doi.org/10.1130/0091-7613(2000)28<995:SYESPI>2.0.CO;2, 2000.

904

905   Cohen, H. and Laronne, J. B.: High rates of sediment transport by flashfloods in the Southern

906   Judean Desert, Israel, Hydrol. Process., 19, 1687–1702, https://doi.org/10.1002/hyp.5630,

907   2005.

908

909   Cools, J., Vanderkimpen, P., El Afandi, G., Abdelkhalek, A., Fockedey, S., El Sammany, M.,

910   Abdallah, G., El Bihery, M., Bauwens, W., and Huygens, M.: An early warning system for

911   flash floods in hyper-arid Egypt, Nat. Hazards Earth Syst. Sci., 12, 443–457, 2012.

912

913 Dayan, U., Ziv, B., Margalit, A., Morin, E. Y., and Sharon, D.: A severe autumn storm over

914 the middle-east : synoptic and mesoscale convection analysis, 122, 103–122,

915 https://doi.org/10.1007/s007040170038, 2001.

916

917 Dayan, U., Ziv, B., Shoob, T., and Enzel, Y.: Suspended dust over southeastern

918 Mediterranean and its relation to atmospheric circulations, Int. J. Climatol., 28, 915–924,

919 https://doi.org/https://doi.org/10.1002/joc.1587, 2008.

920

921 Dayan, U., Lensky, I. M., Ziv, B., and Khain, P.: Atmospheric conditions leading to an

922 exceptional fatal flash flood in the Negev Desert, Israel, Nat. Hazards Earth Syst. Sci., 21,

923 1583–1597, https://doi.org/10.5194/nhess-21-1583-2021, 2021.

924

925 Draper, D. W., Newell, D. A., Wentz, F. J., Krimchansky, S., and Skofronick-Jackson, G. M.:

926 The global precipitation measurement (GPM) microwave imager (GMI): Instrument overview

927 and early on-orbit performance, IEEE J. Sel. Top. Appl. Earth Obs. Remote Sens., 8, 3452–

928 3462, 2015.

929

930 Dunkerley, D. and Brown, K.: Flow behaviour, suspended sediment transport and

931 transmission losses in a small (sub-bank-full) flow event in an Australian desert stream,

932 Hydrol. Process., 13, 1577–1588, 1999.

933

934 El-Fandy, M.G., 1948. The effect of the sudan monsoon low on the development of thundery

935 conditions in Egpyt, Palestine and Syria. Quarterly Journal of the Royal Meteorological

936 Society, 74(319), pp.31-38.

937

938 El-Fandy, M. G.: Effects of Topography and Other Factors on the Movement of Lows in the

939 Middle East and Sudan, Bull. Am. Meteorol. Soc., 31, 375–381, https://doi.org/10.1175/1520-

940 0477-31.10.375, 1950.

941

942 Farhan, Y. and Anaba, O.: Flash Flood Risk Estimation of Wadi Yutum (Southern Jordan)

943 Watershed Using GIS Based Morphometric Analysis and Remote Sensing Techniques, Open

944 J. Mod. Hydrol., 06, 79–100, https://doi.org/10.4236/ojmh.2016.62008, 2016.

945

946

947   Farhan, Y. and Anbar, A.: Fragile Landscape: Impact and Consequences of May 2014 Flash-

948   flood Disaster in the Aqaba Area, Southern Jordan, Res. J. Environ. Earth Sci., 6, 451–465,

949   https://doi.org/10.19026/rjees.6.5257, 2014.

950

951   Gee, G. W. and Hillel, D.: Groundwater recharge in arid regions: Review and critique of

952   estimation methods, Hydrol. Process., 2, 255–266,

953   https://doi.org/https://doi.org/10.1002/hyp.3360020306, 1988.

954

955   Greenbaum, N., Enzel, Y., and Schick, A. P.: Magnitude and frequency of paleofloods and

956   historical floods in the Arava basin, Negev Desert, Israel, Isr. J. Earth Sci., 50, 159–186,

957   https://doi.org/10.1092/N5VU-FU5F-QNWC-UDCK, 2001.

958

959   Haggag, M. and El-Badry, H.: Mesoscale Numerical Study of Quasi-Stationary Convective

960   System over Jeddah in November 2009, Atmos. Clim. Sci., 03, 73–86,

961   https://doi.org/10.4236/acs.2013.31010, 2013.

962

963   Hereford, R., Webb, R. H., and Longpré, C. I.: Precipitation history and ecosystem response

964   to multidecadal precipitation variability in the Mojave Desert region, 1893-2001, J. Arid

965   Environ., 67, 13–34, https://doi.org/10.1016/j.jaridenv.2006.09.019, 2006.

966

967   Hickey, B. M., Kudela, R. M., Nash, J. D., Bruland, K. W., Peterson, W. T., MacCready, P.,

968   Lessard, E. J., Jay, D. A., Banas, N. S., Baptista, A. M., Dever, E. P., Kosro, P. M., Kilcher,

969   L. K., Horner-Devine, A. R., Zaron, E. D., McCabe, R. M., Peterson, J. O., Orton, P. M., Pan,

970   J., and Lohan, M. C.: River Influences on Shelf Ecosystems: Introduction and synthesis, J.

971   Geophys. Res. Ocean., 115, https://doi.org/https://doi.org/10.1029/2009JC005452, 2010.

972

973   Hochman, A., Alpert, P., Kunin, P., Rostkier-Edelstein, D., Harpaz, T., Saaroni, H., and

974   Messori, G.: The dynamics of cyclones in the twentyfirst century: the Eastern Mediterranean

975   as an example, Clim. Dyn., 54, 561–574, https://doi.org/10.1007/s00382-019-05017-3, 2020.

976

977   Hochman, A., Rostkier-Edelstein, D., Kunin, P. et al. Changes in the characteristics of 'wet'
978   and 'dry' Red Sea Trough over the Eastern Mediterranean in CMIP5 climate projections.
979   Theor Appl Climatol 143, 781–794 (2021).

980

981 Hochman, A, Plotnik, T, Marra, F, Shehter, E-R, Raveh-Rubin, S & Magaritz-Ronen, L 2023,

982 'The sources of extreme precipitation predictability; the case of the 'Wet' Red Sea Trough',

983 *Weather and Climate Extremes*, vol. 40, 100564. https://doi.org/10.1016/j.wace.2023.100564

984

985 Holdren, J. P. and Ehrlich, P. R.: Human population and the global environment, Am. Sci.,

986 62, 282–292, 1974.

987

988 Huffman, G. J., Bolvin, D. T., Braithwaite, D., Hsu, K.-L., Joyce, R. J., Kidd, C., Nelkin, E.

989 J., Sorooshian, S., Stocker, E. F., and Tan, J.: Integrated multi-satellite retrievals for the global

990 precipitation measurement (GPM) mission (IMERG), Satell. Precip. Meas. Vol. 1, 343–353,

991 2020.

992

993 Kahana, R., Ziv, B., Enzel, Y., and Dayan, U.: Synoptic climatology of major floods in the

994 Negev Desert, Israel, Int. J. Climatol., 22, 867–882, https://doi.org/10.1002/joc.766, 2002.

995

996 Kalman, A., Katz, T., Hill, P., and Goodman-Tchernov, B.: Droughts in the desert: Medieval

997 Warm Period associated with coarse sediment layers in the Gulf of Aqaba-Eilat, Red Sea,

998 Sedimentology, 67, 3152–3166, https://doi.org/10.1111/sed.12737, 2020.

999

1000 Kalman, A., Goodman-Tchernov, B., Hill, P., Everhardt IV, C., Mathalon, A., and Katz, T.:

1001 Anthropogenic changes in waterways produce "drought-like" layers in shelf sediments, Elem.

1002 Sci. Anthr., 10, 39, https://doi.org/10.1525/elementa.2021.00039, 2022.

1003

1004 Kalnay, E., Kanamitsu, M., Kistler, R., Collins, W., Deaven, D., Gandin, L., Iredell, M., Saha,

1005 S., White, G., Woollen, J., Zhu, Y., Chelliah, M., Ebisuzaki, W., Higgins, W., Janowiak, J.,

1006 Mo, K. C., Ropelewski, C., Wang, J., Leetmaa, A., Reynolds, R., Jenne, R., and Joseph, D.:

1007 The NCEP/NCAR 40-Year Reanalysis Project, Bull. Am. Meteorol. Soc., 77, 437–472,

1008 https://doi.org/10.1175/1520-0477(1996)077<0437:TNYRP>2.0.CO;2, 1996.

1009

1010 Katz, T., Ginat, H., Eyal, G., Steiner, Z., Braun, Y., Shalev, S., and Goodman-Tchernov, B.

1011 N.: Desert flash floods form hyperpycnal flows in the coral-rich Gulf of Aqaba, Red Sea,

1012 Earth Planet. Sci. Lett., 417, 87–98, https://doi.org/10.1016/j.epsl.2015.02.025, 2015.

1013

1014

1015 Kouroutzoglou, J., Flocas, H. A., Hatzaki, M., Keay, K., Simmonds, I., and Mavroudis, A.:

1016 On the dynamics of a case study of explosive cyclogenesis in the Mediterranean, Meteorol.

1017 Atmos. Phys., 127, 49–73, 2015.

1018

1019 Krichak, S. O. and Alpert, P.: Role of large scale moist dynamics in November 1-5, 1994,

1020 hazardous Mediterranean weather, J. Geophys. Res. Atmos., 103, 19453–19468,

1021 https://doi.org/10.1029/98JD01710, 1998.

1022

1023 Krichak, S. O., Breitgand, J. S., and Feldstein, S. B.: A conceptual model for the identification

1024 of active Red Sea trough synoptic events over the southeastern Mediterranean, J. Appl.

1025 Meteorol. Climatol., 51, 962–971, 2012.

1026

1027 Lekach, J. and Schick, P.: Suspended sediment in desert floods in small catchments, Isr. J.

1028 Earth-Sciences, 31, 144–156, 1982.

1029

1030 Loya, Y.: The coral reefs of Eilat—past, present and future: three decades of coral community

1031 structure studies, in: Coral health and disease, Springer, 1–34, 2004.

1032

1033 Masaki, T., Kubota, T., Oki, R., Kojima, M., Furukawa, K., Miura, T., Kai, H., Iguchi, T.,

1034 Hanado, H., and Yoshida, N.: Development of level 1 algorithm of dual frequency

1035 precipitation radar (DPR) for the global precipitation measurement (GPM), in: 2014 IEEE

1036 Geoscience and Remote Sensing Symposium, 4962–4965, 2014.

1037

1038 Mathalon, A., Goodman-Tchernov, B., Hill, P., Kálmán, Á., and Katz, T.: Factors influencing

1039 flashflood deposit preservation in shallow marine sediments of a hyperarid environment, Mar.

1040 Geol., 411, 22–35, https://doi.org/10.1016/j.margeo.2019.01.010, 2019.

1041

1042 Merz, B., Blöschl, G., Vorogushyn, S., Dottori, F., Aerts, J. C. J. H., Bates, P., Bertola, M.,

1043 Kemter, M., Kreibich, H., Lall, U., and Macdonald, E.: Causes, impacts and patterns of

1044 disastrous river floods, Nat. Rev. Earth Environ., 2, 592–609, https://doi.org/10.1038/s43017-

1045 021-00195-3, 2021.

1046

1047 Milliman, J. D. and Farnsworth, K. L.: River discharge to the coastal ocean: a global

1048 synthesis, Cambridge University Press, 2013.

1049 Mohammed, S. A., Hamouda, M. A., Mahmoud, M. T., and Mohamed, M. M.: Performance

1050 of GPM-IMERG precipitation products under diverse topographical features and multiple-

1051 intensity rainfall in an arid region, Hydrol. Earth Syst. Sci. Discuss., 2020, 1–27, 2020.

1052

1053 Mulder, T., Syvitski, J. P. M., Migeon, S., Faugères, J. C., and Savoye, B.: Marine

1054 hyperpycnal flows: Initiation, behaviorand related deposits. A review, Mar. Pet. Geol., 20,

1055 861–882, https://doi.org/10.1016/j.marpetgeo.2003.01.003, 2003.

1056

1057 Mullenbach, B. L. and Nittrouer, C. A.: Rapid deposition of fluvial sediment in the Eel

1058 Canyon, northern California, Cont. Shelf Res., 20, 2191–2212,

1059 https://doi.org/https://doi.org/10.1016/S0278-4343(00)00067-4, 2000.

1060

1061 Neumann, B., Vafeidis, A. T., Zimmermann, J., and Nicholls, R. J.: Future coastal population

1062 growth and exposure to sea-level rise and coastal flooding - A global assessment, PLoS One,

1063 10, https://doi.org/10.1371/journal.pone.0118571, 2015.

1064

1065 Nguyen, P., Shearer, E., Ombadi, M., Gorooh, V., Hsu, K., Sorooshian, S., Logan, W. and

1066 Ralph, M. (2020). PERSIANN Dynamic Infrared–Rain Rate Model (PDIR) for High-

1067 Resolution, Real-Time Satellite Precipitation Estimation. *Bulletin of the American*

1068 *Meteorological Society* 101(3) pp. E286-E302. Available at:

1069 https://journals.ametsoc.org/view/journals/bams/101/3/bams-d-19-0118.1.xml.

1070

1071 Parsons, J. D., Bush, J. W. M., and Syvitski, J. P. M.: Hyperpycnal plume formation from

1072 riverine outflows with small sediment concentrations, Sedimentology, 48, 465–478, 2001.

1073

1074 Pradhan, R. K., Markonis, Y., Godoy, M. R. V., Villalba-Pradas, A., Andreadis, K. M.,

1075 Nikolopoulos, E. I., Papalexiou, S. M., Rahim, A., Tapiador, F. J., and Hanel, M.: Review of

1076 GPM IMERG performance: A global perspective, Remote Sens. Environ., 268, 112754, 2022.

1077

1078 Reid, I. and Frostick, L. E.: Flow dynamics and suspended sediment properties in arid zone

1079 flash floods, Hydrol. Process., 1, 239–253,

1080 https://doi.org/https://doi.org/10.1002/hyp.3360010303, 1987.

1081

1082

1083   Saaroni, H., Harpaz, T., Alpert, P., and Ziv, B.: Automatic identification and classification of

1084   the northern part of the Red Sea trough and its application for climatological analysis, Int. J.

1085   Climatol., 40, 3607–3622, https://doi.org/10.1002/joc.6416, 2020.

1086

1087   Saligheh, M.: The Effect of Merging Subtropical Jet Stream and Polar Fronts Jet Stream on

1088   Heavy Rainfall in Southwest Asia, 2021.

1089

1090   Schick, A. P. and Lekach, J.: An evauation of two ten-year sediment budgets, Nahal Yael,

1091   Israel, Phys. Geogr., 14, 225–238, https://doi.org/10.1080/02723646.1993.10642477, 1993.

1092

1093   Shalash, S.: Effects of sedimentation on the storage capacity of the High Aswan Dam

1094   reservoir, Hydrobiologia, 91–92, 623–639, https://doi.org/10.1007/BF00000061, 1982.

1095

1096   Sharon, D.: The spottiness of rainfall in a desert area, J. Hydrol., 17, 161–175,

1097   https://doi.org/https://doi.org/10.1016/0022-1694(72)90002-9, 1972.

1098

1099   Shentsis, I., Meirovich, L., Ben-Zvi, A., and Rosenthal, E.: Assessment of transmission losses

1100   and groundwater recharge from runoff events in watercourses of the Neqarot watershed,

1101   Israel, Isr. J. Earth Sci., 50, 201–215, https://doi.org/10.1092/J79L-39QP-NC9G-WFTF,

1102   2001.

1103

1104   Small, C. and Nicholls, R.: A Global Analysis of Human Settlement in Coastal Zones, J.

1105   Coast. Res., 19, https://doi.org/10.2307/4299200, 2003.

1106

1107   Syvitski, J. P. M., Vörösmarty, C. J., Kettner, A. J., and Green, P.: Impact of humans on the

1108   flux of terrestrial sediment to the global coastal ocean, Science (80-.)., 308, 376–380,

1109   https://doi.org/10.1126/science.1109454, 2005.

1110

1111   Tapiador, F. J., Navarro, A., García-Ortega, E., Merino, A., Sánchez, J. L., Marcos, C., and

1112   Kummerow, C.: The contribution of rain gauges in the calibration of the IMERG product:

1113   Results from the first validation over Spain, J. Hydrometeorol., 21, 161–182, 2020.

1114

1115   Tsvieli, Y. and Zangvil, A.: Synoptic climatological analysis of "wet" and "dry" Red Sea

1116   Troughs over Israel, Int. J. Climatol., 25, 1997–2015, https://doi.org/10.1002/joc.1232, 2005.

de Vries, A. J., Ouwersloot, H. G., Feldstein, S. B., Riemer, M., El Kenawy, A. M., McCabe, M. F., and Lelieveld, J.: Identification of Tropical-Extratropical Interactions and Extreme Precipitation Events in the Middle East Based On Potential Vorticity and Moisture Transport, J. Geophys. Res. Atmos., 123, 861–881, https://doi.org/10.1002/2017JD027587, 2018.

De Vries, A. J., Tyrlis, E., Edry, D., Krichak, S. O., Steil, B., and Lelieveld, J.: Extreme precipitation events in the Middle East: Dynamics of the Active Red Sea Trough, J. Geophys. Res. Atmos., 118, 7087–7108, https://doi.org/10.1002/jgrd.50569, 2013.

Walters, M. O.: Transmission losses in arid region, J. Hydraul. Eng., 116, 129–138, 1990.

Yang, H. F., Yang, S. L., Xu, K. H., Milliman, J. D., Wang, H., Yang, Z., Chen, Z., and Zhang, C. Y.: Human impacts on sediment in the Yangtze River: A review and new perspectives, Glob. Planet. Change, 162, 8–17, https://doi.org/10.1016/j.gloplacha.2018.01.001, 2018.

Youssef, A. M., Sefry, S. A., Pradhan, B., and Alfadail, E. A.: Analysis on causes of flash flood in Jeddah city (Kingdom of Saudi Arabia) of 2009 and 2011 using multi-sensor remote sensing data and GIS, Geomatics, Nat. Hazards Risk, 7, 1018–1042, https://doi.org/10.1080/19475705.2015.1012750, 2016.

Zirks, E., Krom, M., Schmiedl, G., Katz, T., Xiong, Y., Alcott, L. J., Poulton, S. W., and Goodman-Tchernov, B.: Redox evolution and the development of oxygen minimum zones in the Eastern Mediterranean Levantine basin during the early Holocene, Geochim. Cosmochim. Acta, 297, 82–100, https://doi.org/10.1016/j.gca.2021.01.009, 2021.

Ziv, B., Dayan, U., and Sharon, D.: A mid-winter, tropical extreme flood-producing storm in southern Israel: Synoptic scale analysis, Meteorol. Atmos. Phys., 88, 53–63, https://doi.org/10.1007/s00703-003-0054-7, 2005.

Ziv, B., Harpaz, T., Saaroni, H., and Blender, R.: A new methodology for identifying daughter cyclogenesis: Application for the Mediterranean Basin, Int. J. Climatol., 35, 3847–3861, https://doi.org/10.1002/joc.4250, 2015.

1151   Ziv, B., Shimer, R., Harpaz, T., Drori, R., Alpert, P., Raveh-Rubin, S., and Saaroni, H.:

1152   Identification and classification of the wet Red Sea Trough over Israel, Int. J. Climatol., 42,

1153   10062–10082, https://doi.org/10.1002/joc.7884, 2022.

1154

1155